Journal of Geophysical Research: Oceans

RESEARCH ARTICLE

Special Section:
Physical Processes Responsible for Material Transport in the Gulf of Mexico for Oil Spill Applications

Key Points:
- Deformation is decomposed into dilation (area changing) and stretch (area preserving)
- Dilation is a reliable diagnostic tool for identifying cluster locations
- Material accumulation can be quantified using the cluster strength metric

Correspondence to:
H.S. Huntley,
helgah@udel.edu

Clusters, deformation, and dilation: Diagnostics for material accumulation regions

Helga S. Huntley[1], B. L. Lipphardt Jr.[2], Gregg Jacobs[3], and A. D. Kirwan Jr.[1]

[1]School of Marine Science and Policy, University of Delaware, Newark, Delaware, USA, [2]Formerly at School of Marine Science and Policy, University of Delaware, Newark, Delaware, USA, [3]Naval Research Laboratory, Stennis Space Center, Mississippi, USA

Abstract Clusters of material at the ocean surface have been frequently observed. Such accumulations of material play an important role in a variety of applications, from biology to pollution mitigation. Identifying where clusters will form can aid in locating, for example, hotspots of biological activity or regions of high pollutant concentration. Here cluster strength is introduced as a new metric for defining clusters when all particle positions are known. To diagnose regions likely to contain clusters without the need to integrate millions of particle trajectories, we propose to use dilation, which quantifies area changes of Lagrangian patches. Material deformation is decomposed into dilation and area-preserving stretch processes to refine previous approaches based on finite-time Lyapunov exponents (FTLE) by splitting the FTLE into fundamental kinematic properties. The concepts are developed theoretically and illustrated in the context of a state-of-the-art data-assimilating predictive ocean model of the Gulf of Mexico. Regions of dilation less than one are shown to be much more likely (6 times more likely in the given example) to be visited by particles than those of dilation greater than one. While the relationship is nonlinear, dilation and cluster strength exhibit a fairly good correlation. In contrast, both stretch and Eulerian divergence are found to be uncorrelated with cluster strength. Thus, dilation maps can be used as guides for identifying cluster locations, while saving some of the computational cost of trajectory integrations.

1. Introduction

The nonuniform distribution of material at the ocean surface has long been cause for fascination [e.g., *Day and Shaw*, 1987; *Yoder et al.*, 1994; *Toner et al.*, 2003; *Lebreton et al.*, 2012]. The much documented "garbage patch" in the Pacific Ocean may be the most prominent example of this phenomenon [*Kaiser*, 2010; *Howell et al.*, 2012]. More recently, the abundant availability of satellite imagery confirms that cluster patterns in the distribution of materials such as chlorophyll or oil are not isolated curiosities but commonplace in many parts of the world's oceans. Figure 1 shows some examples. Here "cluster" is used loosely as an accumulation of material with higher density than in surrounding areas; a rigorous definition is provided in section 3.

To a good approximation, ocean flows are incompressible. Thus, there is no obvious mechanism for uniformly distributed, neutrally buoyant particles to cluster. However, floating particles experience the convergence and divergence in the two-dimensional flow field resulting from downwelling and upwelling. The modeling study of *Zhong et al.* [2012] showed that buoyant particles advected with the ocean flows preferentially occupy locations with instantaneous convergence. This result is intuitive for stationary or slowly evolving flows, where the Lagrangian time scales associated with particle motion are much smaller than the Eulerian time scales associated with flow evolution.

When submesoscale flows are considered, where the Lagrangian and Eulerian time scales may be comparable, the instantaneous state of the velocity field may be less useful as a predictor of cluster locations. *Zhong et al.* [2012] in fact did not consider the predictive power of the divergence field for particle accumulation patterns.

One approach to describing transport patterns, sometimes thought of as "highways" and "parking lots" for advected material, that has become widespread over the last two decades is the mapping of Lagrangian coherent structures (LCS). These are frequently taken as ridges in maps of the finite-time or finite-space Lyapunov exponents (FTLE and FSLE, respectively) [e.g., *Boffetta et al.*, 2001; *d'Ovidio et al.*, 2004; *Shadden et al.*, 2005;
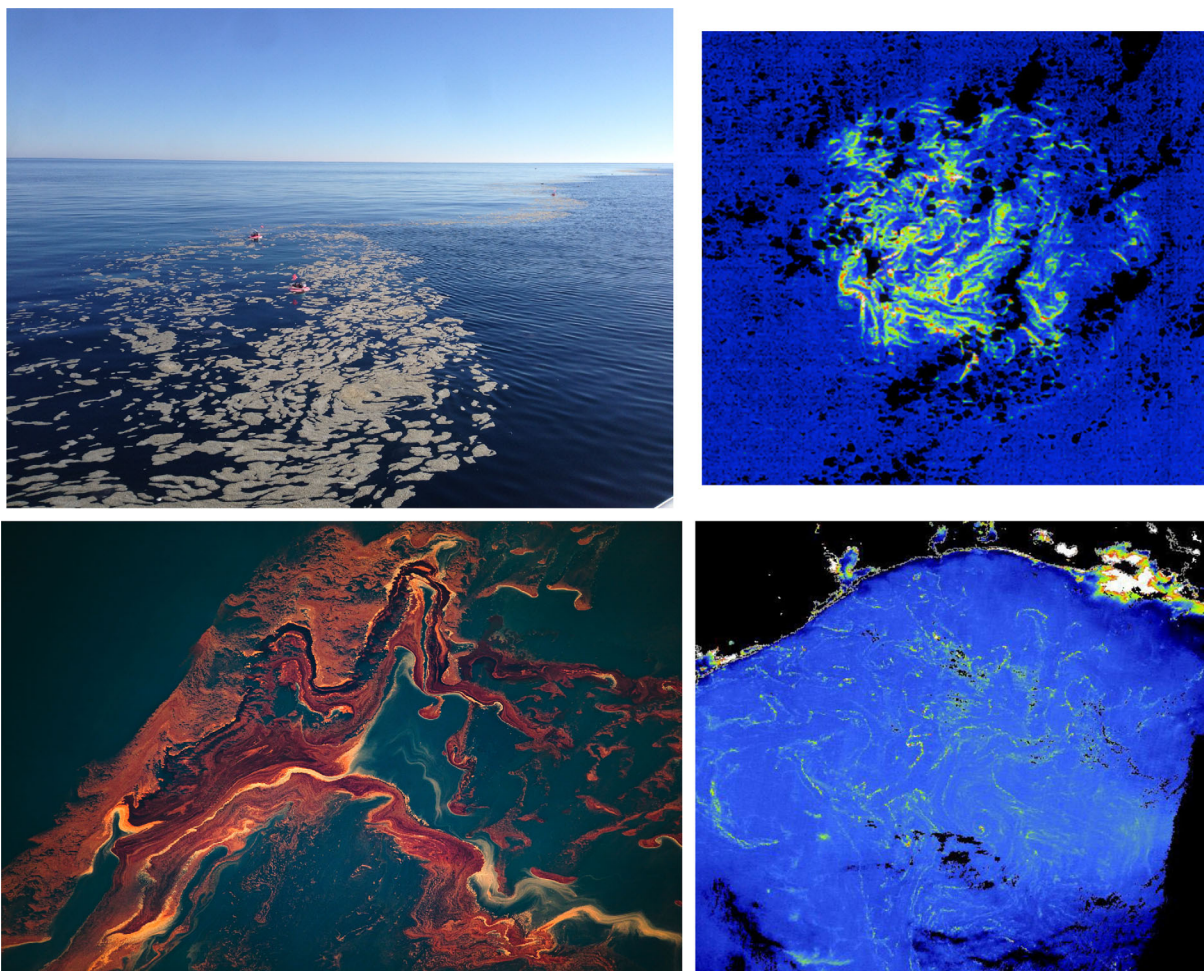
Figure 1. (top left) A cluster of surface drifters and Sargassum along a front in the northeastern Gulf of Mexico. (Image courtesy Tamay Özgökmen.) (bottom left) Accumulating oil from the *Deepwater Horizon* oil spill in the Gulf of Mexico. (Photo by Daniel Beltrá.) (top right) Patch of sargassum off the east coast of U.S., as observed by Envisat. (Image courtesy ESA.) (bottom right) Streaks of sargassum in the western Gulf of Mexico, as observed by MERIS. (Image courtesy ESA.)

Rypina et al., 2010; *Harrison and Glatzmaier*, 2012], although other techniques have been suggested [*Mendoza and Mancho*, 2010; *Mezić et al.*, 2010; *Haller and Beron-Vera*, 2012]. LCS are used to identify flow regime boundaries and areas of large deformation [*Samelson*, 2013]. Generally, they are expected to be more robust to model error than individual or even groups of trajectory forecasts [*Haller*, 2002; *Hernández-Carrasco et al.*, 2011; *Huntley et al.*, 2011]. LCS have been found to be useful in the context of pollution mitigation in the ocean in that they can indicate preferred pathways and areas of decreased predictability [*Coulliette et al.*, 2007; *Huntley et al.*, 2011; *Olascoaga and Haller*, 2012].

Nevertheless, it remains unclear whether LCS are an adequate diagnostic for clusters. Their clear advantage over Eulerian quantities such as divergence for this purpose is that they capture a particle's or patch's history. Accumulation after all is not an instantaneous process. LCS characterize net deformation properties, and deformation can be separated into area changes and area-preserving stretch (see section 4). Much of the theory underlying LCS has been developed in the context of divergence-free flows [*Haller and Yuan*, 2000; *Boffetta et al.*, 2001; *Haller*, 2001; *Mancho et al.*, 2006]. Yet without divergence, particle densities cannot change (except due to finite sampling phenomena) and clusters will not form. It is thus natural to look for alternatives that capture a particle's history of divergence but separate out stretch effects. A logical candidate is the along-track integral of divergence. This is closely related to what we will call "dilation" (see precise definition in section 4). Integrated over a patch, dilation gives the ratio of final to initial patch area.

This study seeks to show how patterns in dilation relate to patterns visible in the distribution of advected particles. Its advantages over both FTLE and instantaneous divergence as a diagnostic for clusters are

demonstrated. To do so, more than a million floating particles are simulated in a state-of-the-art regional ocean model. However, to move beyond a purely visual comparison, a metric is also needed to identify clusters and to differentiate clusters of greater and lesser density. Counting particles in grid boxes is a common approach [*Schumacher and Eckhardt*, 2002; *Boffetta et al.*, 2004; *Cressman et al.*, 2004], but suffers from its dependence on a grid and, in particular, the orientation of the grid. Thus, we introduce a grid-independent cluster strength function as an alternative.

The model experiment is briefly described in section 2, followed by a discussion of how to define clusters and clustering rigorously in section 3. Section 4 contains the theoretical development of dilation, placing it into the context of other diagnostics. Numerical details are relegated to Appendix A. Section 5 presents the analysis of the diagnostics for material accumulation regions. A summary and conclusions are provided in section 6.

2. Model Description

To illustrate the concepts of clustering and dilation and to explore their relationship in a realistic ocean setting, we make use of the Navy Coastal Ocean Model (NCOM) in its regional configuration maintained at the Naval Research Laboratory [*Barron et al.*, 2006]. The domain consists of the entire Gulf of Mexico and extends to the eastern shore of Florida and south of the Yucatan Strait, ranging from 98°W to 79°W and from 18°N to 31°N. The boundary conditions are supplied by a global implementation of NCOM run with 1/8° resolution [*Barron et al.*, 2007]. The horizontal resolution is roughly 3 km. There are 50 vertical layers, with 16 z-levels below 550 m and 34 σ-levels above that. The surface layer, which is used for the analyses presented here, has a nominal thickness of 0.5 m. Surface boundary forcing is taken from the Coupled Ocean/Atmosphere Mesoscale Prediction System (COAMPS) [*Hodur et al.*, 2002; *Hodur*, 1997]. River input is simulated through climatological monthly means, which are set at the center of each month and then interpolated in time for other days.

The particular model run used here for the summer of 2012 was initialized on 1 May 2012. Sea surface height and temperature observations from satellites, as well as any available in situ observations are assimilated using a 3DVar approach in the Navy Coupled Ocean Data Assimilation (NCODA) system [*Cummings*, 2005]. The model was run in real time, so that data latency may have impacted the analyses. Model output was stored at 3 h intervals and is publicly available under doi number 10.7266/N72Z13F4.

The example used throughout this paper focuses on a group of roughly 1.4 million particles launched on a 1 km grid extending from 95°W to 82°W and from 20°N to the coastline near 30°N on 15 July 2012, 00:00. These were advected by the modeled flow for 10 days using a fourth-order Runge-Kutta scheme with a 10 min time step. The analysis is performed on the region between 91°W and 86°W and between 24°N and 28°N.

The experiment was repeated using the geostrophic surface velocities implied by the model's sea surface height field Ψ. These were computed using an *f*-plane approximation and the equations

$$u_g = -\frac{g}{f}\frac{\partial \Psi}{\partial y},\tag{1}$$

$$v_g = \frac{g}{f}\frac{\partial \Psi}{\partial x},\tag{2}$$

where g is the gravitational constant and f is a mean value of the Coriolis parameter for the domain.

3. What is Clustering? An Objective Definition

Clustering is visually easily identified (Figure 1), but to our knowledge, lacks a standard rigorous definition. In some sense, a cluster is an accumulation of particles or material. The process of clustering is then the formation of clusters. There are various mathematical techniques for identifying clusters in a data set, including hierarchical clustering [*Johnson*, 1967], expectation maximization clustering [*Dempster et al.*, 1977], and *k*-means clustering [*Lloyd*, 1982]. The last of these has previously been successfully employed for identifying

drifter clusters to derive oceanographic flow properties [*Koszalka and LaCasce*, 2010; *Koszalka et al.*, 2011]. Many of these techniques rely on parameters that define maximum spacing within a cluster or the target number of clusters. In the context of particles aggregating on the ocean surface, these parameters are difficult to set a priori. Moreover, it is also desirable to assign a degree of clustering to every particle that differentiates small and large clusters, but also dense and loose clusters.

One possible cluster metric is the particle density, defined as the count of particles in each box of a grid overlaid on the domain of interest, as mentioned above. The resolution of the resulting particle density field is necessarily limited to the chosen grid resolution, and if the grid is refined too much, the particle density becomes binary. Moreover, the orientation of the grid, either aligning with cluster lines or not, can influence the result. Particle density is restricted to integer values, sacrificing the nuance available to continuous metrics. Most importantly for the purposes here, it is insensitive to clusters extending beyond a grid box or the density of a cluster within a grid box.

Another metric is the inverse of the area of Voronoï cells [*Monchaux et al.*, 2010; *Fiabane et al.*, 2012]. A Voronoï diagram divides a domain into cells, such that each cell contains one particle and all the points closer to this particle than to any other. It avoids the need for a predefined length scale or grid dependence. On the other hand, this method cannot distinguish between particles surrounded by a few and those surrounded by many nearby particles.

To overcome some of these shortcomings, we propose here the cluster strength C defined for any location $\boldsymbol{x}^*$ as

$$C(\boldsymbol{x}^*) = \sum_{n=1}^{N} e^{-(d_n/L)^2}, \tag{3}$$

where

$$d_n = |\boldsymbol{x}_n - \boldsymbol{x}^*|, \tag{4}$$

is the distance from the location $\boldsymbol{x}^*$ to the nth particle at $\boldsymbol{x}_n$, and L is a tunable length-scale parameter. One can interpret $C(\boldsymbol{x}^*)$ as a weighted sum of all particles, where the weights are a function of the distance from $\boldsymbol{x}^*$. The shape of the weighting function, i.e., the discount rate for far-away particles, is determined by L. A reasonable choice for L, and the one used in the analysis below, is half the mean spacing of the particles if they were distributed uniformly.

Like all other metrics, C does have some undesirable properties. In this case, they are related to edge effects on a finite, nonperiodic domain. On such a domain, even equally spaced particles on a grid will yield a non-uniform cluster strength field: in a strip along the boundaries, with a length scale of $2L$, the cluster strength is reduced. One way to avoid these biases is to extend the computational domain beyond the analysis domain. This must be done anyway to ensure an inflow of particles through open boundaries. Otherwise, artificial voids are created that bias the results.

It should also be noted that the cluster strength C is not strictly conserved. Each particle's influence extends to infinity (although it is small outside a radius of $2L$). As particles travel closer to or farther from the boundary of the domain, different portions of the Gaussian weight fall inside the domain. On the other hand, particles that have crossed out of the analysis domain but remain within the computational domain continue to be counted, unlike for particle density defined by grid counts.

While the analysis of this study is restricted to finite collections of discrete particles, the concept of cluster strength can easily be extended to a continuous tracer with concentration ρ. Denoting the domain by Ω, the cluster strength is given by

$$C(\boldsymbol{x}^*) = \iint_{\Omega} \rho(\boldsymbol{x}) e^{-[d(\boldsymbol{x})/L]^2} \, d\boldsymbol{x}, \tag{5}$$

where

$$d(\boldsymbol{x}) = |\boldsymbol{x} - \boldsymbol{x}^*|, \tag{6}$$

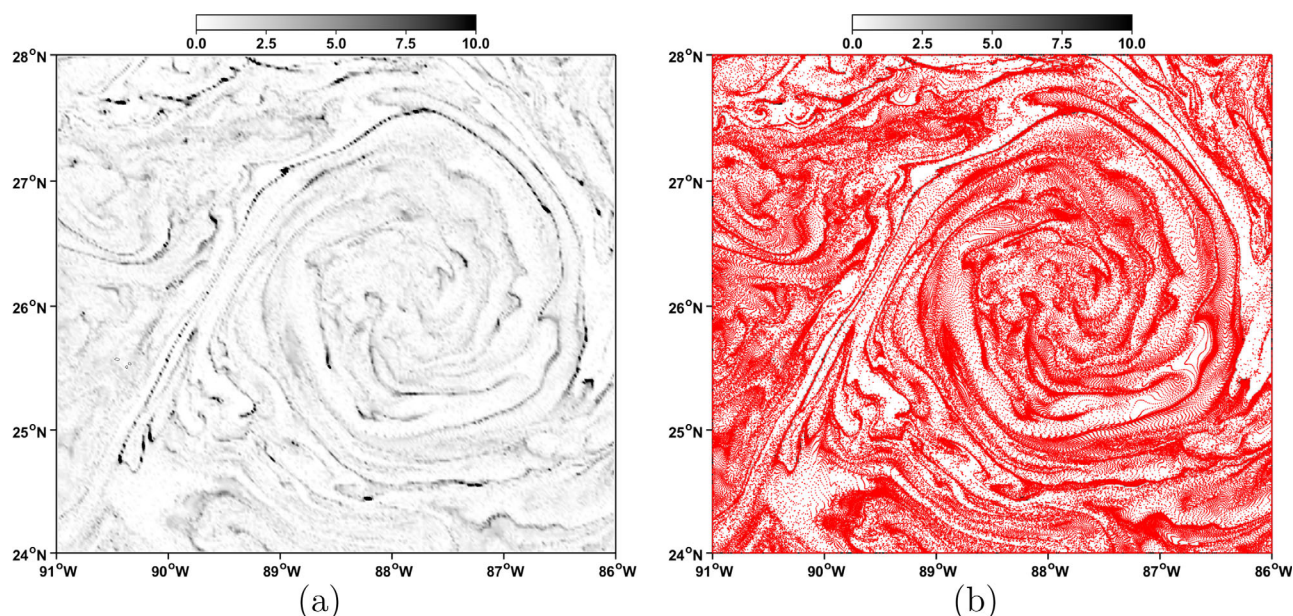is the distance from $\boldsymbol{x}^*$ to $\boldsymbol{x}$.

Figure 2. (a) Cluster strength on 25 July 2012 00:00, computed on a 2 km grid from particles launched on a 1 km grid 10 days before. (b) The same with particle positions overlaid in red.

The main advantages of cluster strength as a metric are: (1) It is independent of any grid. (2) It differentiates degrees of aggregation. (3) Its only parameter can be determined a priori based on the length scales of interest. Like all clustering metrics, the cluster strength is a function of the particle positions. Thus, the initial positions and integration length for the particle trajectories will critically affect the cluster strength field.

An illustration of the application of cluster strength is given in Figure 2. Given the ≈ 1.4 million trajectories from the main experiment outlined in section 2, C was computed at the end of the 10 day integration on a 2 km grid, nested inside the domain used for the trajectory calculations, using a length scale of $L = 0.5$ km. The ridges in cluster strength shown in Figure 2a clearly coincide with the visually identifiable "clusters" of particles shown in Figure 2b.

Now we can rigorously and objectively define a "cluster" as a region of locally higher cluster strength C, and "clustering" as the increasing of cluster strength over time.

While many observations of cluster patterns exist, especially from satellite and airborne images (e.g., Figure 1), it is well established, theoretically [Sawford, 2001, and references therein], numerically [Poje et al., 2010], and observationally [Poje et al., 2014], that, on average, floating particles tend to disperse. This may appear as a contradiction. However, the rearrangement of initially uniformly distributed particles into a distribution with significant peaks in C also requires the creation of voids, or areas with locally lower cluster strength. The eye is drawn to the clusters, but the particle pair statistics are heavily influenced by the large separations at the virtually unbounded upper end of the distribution.

Cressman et al. [2004] illustrated this statistical phenomenon nicely by showing the evolving probability distribution of particle separations, starting from an initially uniform distribution, in a numerical model of a 3-D turbulent flow (see their Figure 11). A similar analysis for the model used here shows similar results (Figure 3). At launch, the probability distribution is a delta function centered at 1 km (Figure 3a). Over time, it flattens out, with both the mean and the median increasing (Figure 3c), consistent with relative dispersion in the average behavior. Simultaneously, the probabilities of low separation distances increase as well (Figure 3b), which reflects the appearance of clusters.

Note that the identity of close-by pairs changes. For example, while the total number of pairs closer than 575 m remains almost constant between 3 and 10 days of integration, only 28% of the pairs in this group after 3 days remain in it after 10 days. Thus, pairs approach each other, separate, and come closer again. This indicates that clusters form, breakup, and reform with new constituents as well.
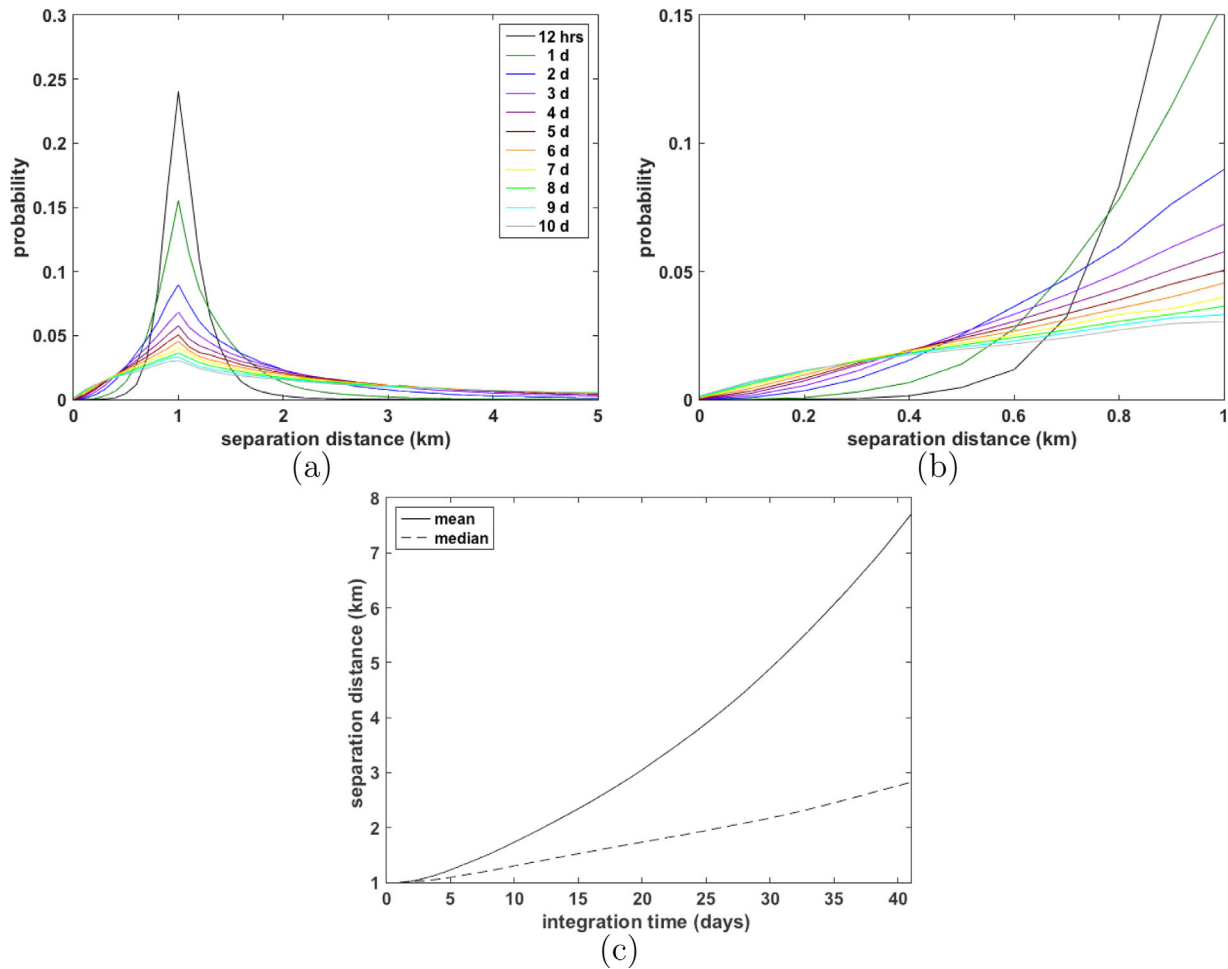
Figure 3. (a and b) Probability distribution of pair separations over time. Each colored line corresponds to a particular integration time. Pairs are defined on the original grid, whereby each particle is partnered with the nearest particle to the north of it. Probabilities are computed using bins with 100 m width. Some separation distances at the later times exceed 600 km; for clarity, two excerpts of the full distribution are shown. (c) Time series of the mean and median separation distances.

4. Dilation, Stretch, and Finite-Time Lyapunov Exponents: Definitions and Theory

Material accumulation is a form of deformation of the initial material patch. There are three types of deformation of a 2-D patch: deformation that retains the area and shape of the patch (rotation), deformation that changes the area of the patch but retains its shape (dilation), and that which keeps the area of the patch constant but changes its shape (stretch). Of course, they usually act together resulting in both area and shape changes. The filamentation observed in images such as Figures 1 and 2b generally results from a combination. A change in density must be caused by dilation, but the resulting clusters are also stretched into complex shapes and rotated into different orientations. Orientation is not of concern in the present context; so rotation will not be considered further.

To make these notions more precise, consider the flow given by

$$\dot{\boldsymbol{x}} = \boldsymbol{u}(\boldsymbol{x}, t) \quad \boldsymbol{x} \in \Omega \subset \mathbb{R}^2, t \in [t_0, T], \tag{7}$$

where $\boldsymbol{u}$ is a smooth velocity field and Ω is an open subset of $\mathbb{R}^2$. (The concepts below can be extended to 3-D, but this is not considered here.) The trajectory of a particle with initial position $\boldsymbol{x}_o$ at time t_o is then given by

$$\boldsymbol{x}(t; t_0, \boldsymbol{x}_0) = \boldsymbol{x}_0 + \int_{t_0}^{t} \boldsymbol{u}(\boldsymbol{x}, \tau) d\tau. \tag{8}$$

Material deformation is captured by the deformation tensor

$$\boldsymbol{F} = \frac{\partial \boldsymbol{x}}{\partial \boldsymbol{x}_0} = \begin{bmatrix} \dfrac{\partial x}{\partial x_o} & \dfrac{\partial x}{\partial y_o} \\[2mm] \dfrac{\partial y}{\partial x_o} & \dfrac{\partial y}{\partial y_o} \end{bmatrix}. \tag{9}$$

$\boldsymbol{F}$ is a linearization of the flow map in $\boldsymbol{x}_o$. Its effects on an infinitesimal fluid patch can be described by its singular value decomposition. Under a linear map, a circle is mapped into an ellipse, and the singular values $\mu_1 \geq \mu_2$ provide the lengths of the semimajor and the semiminor axes of the image ellipse, respectively. The area of the ellipse is $\pi \mu_1 \mu_2$. In fact, in general, for any nonlinear flow, the area of a deformed patch Ω, evolved from Ω_o, is

$$A = \iint_\Omega d\boldsymbol{x} = \iint_{\Omega_o} |\det(\boldsymbol{F})|\, d\boldsymbol{x}_o = \iint_{\Omega_o} \mu_1 \mu_2\, d\boldsymbol{x}_o. \tag{10}$$

Thus, we define *dilation* as the product of the singular values of $\boldsymbol{F}$:

$$\delta = \mu_1 \mu_2. \tag{11}$$

Shape changes under a linear map can be summarized by the eccentricity or the ellipticity of the image ellipse. Both of these are functions of the ratio of the major to the minor axis lengths. Generalizing this concept to an arbitrary flow, we define *stretch* as the ratio of the singular values of $\boldsymbol{F}$:

$$\sigma = \frac{\mu_1}{\mu_2}. \tag{12}$$

Both dilation and stretch are functions of t, and the longer a patch in the flow evolves, the more it is expected to deform. Consequently, in some cases, it is desirable to consider dilation and stretch *rates*. These are defined, respectively, as

$$\Delta = \frac{\log(\delta)}{t}, \tag{13}$$

$$\Sigma = \frac{\log(\sigma)}{t}. \tag{14}$$

As mentioned above, a popular approach to describing transport patterns considers ridges in the finite-time Lyapunov exponent (FTLE) field. The FTLE captures relative dispersion behavior of particles as an exponential separation rate. It is defined as a function of the leading singular value of $\boldsymbol{F}$:

$$\text{FTLE} = \frac{\log(\mu_1)}{t}. \tag{15}$$

From equations (1–15), it follows that

$$\text{FTLE} = \frac{\Delta + \Sigma}{2}. \tag{16}$$

The separation rate is the average of the dilation and the stretch rates. Dilation and stretch, thus, constitute a decomposition of the FTLE, which permits separating processes resulting in area changes from those resulting in shape changes.

Dilation also has an interesting relationship with Eulerian divergence $\nabla \cdot \boldsymbol{u}$. It can be shown that the material derivative of dilation satisfies

$$\frac{D\delta}{Dt} = \delta \nabla \cdot \boldsymbol{u}, \tag{17}$$

from which it follows that

$$\delta(t) = \exp\left\{ \int_0^t \nabla \cdot \boldsymbol{u}[\boldsymbol{x}(\tau), \tau]\, d\tau \right\}, \tag{18}$$

where the integral is taken along trajectories. Along with equation (13), this yields the result that
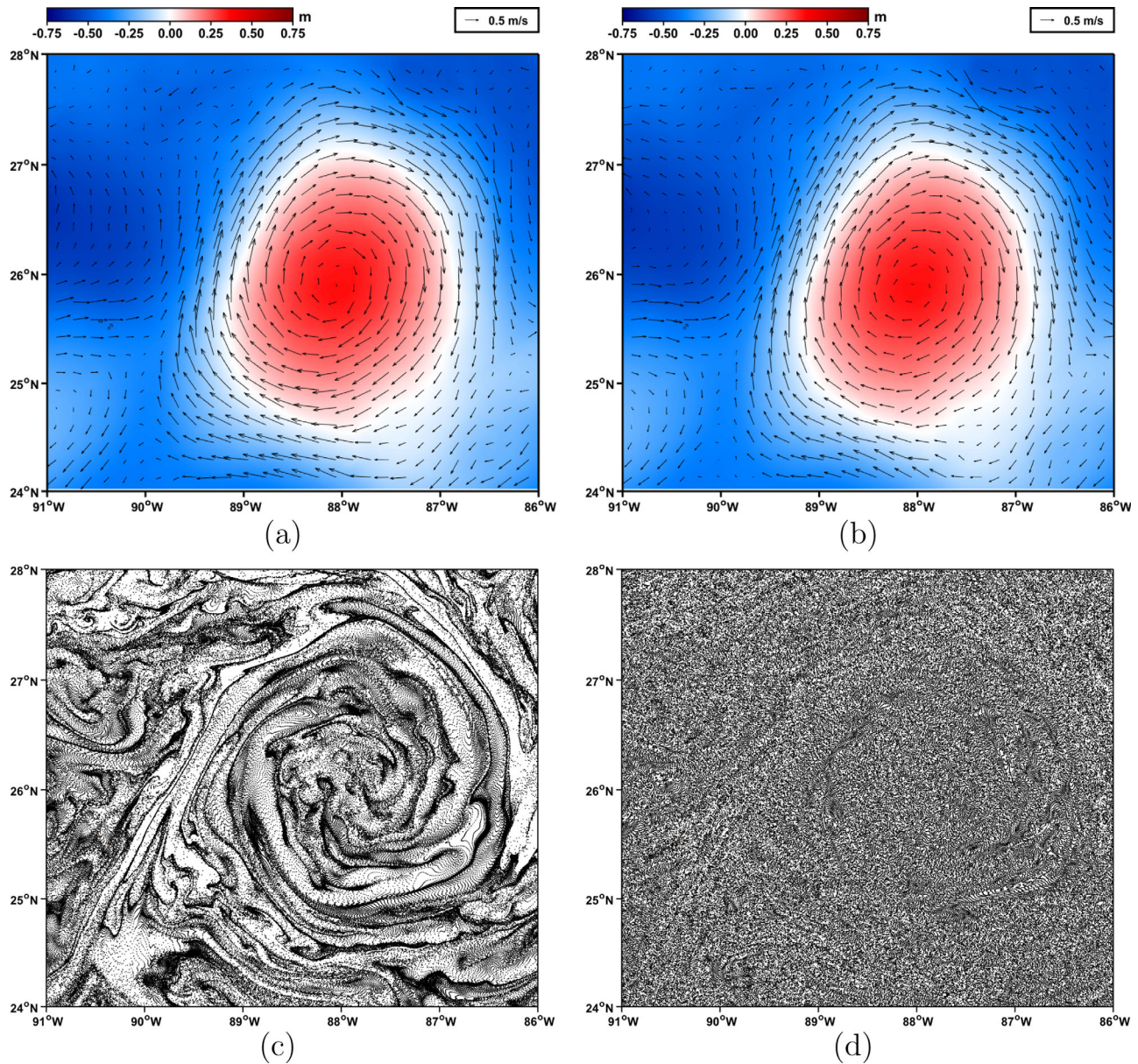
Figure 4. (top) Sea surface height anomaly on 20 July 2012 00:00 with (a) the full velocity field and (b) the geostrophic velocity field. (bottom) Positions of particles launched on a 1 km grid on 15 July 2012 00:00, after 10 days of integration of (c) the full velocity field and (d) the geostrophic velocity field.

$$\Delta = \frac{1}{t} \int_0^t \nabla \cdot \boldsymbol{u}[\boldsymbol{x}(\tau), \tau] \, d\tau, \tag{19}$$

i.e., the dilation rate is the average divergence experienced by a particle along its trajectory.

5. Cluster Diagnostics

Above we stated that material accumulation requires dilation less than 1 and hence nonzero divergence. If $\nabla \cdot \boldsymbol{u} = 0$, then by equation (18), $\delta = 1$ and by equation (10), the area of any patch stays constant. Under these conditions, material cannot accumulate. Particle clustering has previously been reported in incompressible flows, but this is somewhat misleading, since either a random component is added to the incompressible velocity field [*Klyatskin and Saichev*, 1997] or inertial particles are modeled [*Boffetta et al.*, 2004; *Fiabane et al.*, 2012]. In either case, a compressible part is introduced into the particles' Lagrangian velocity.
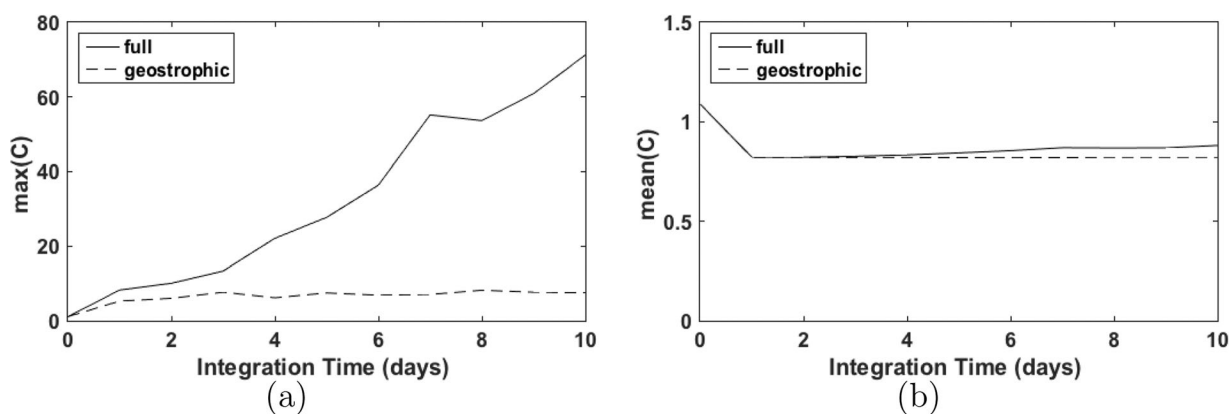
Figure 5. Time series of (a) max (C) and (b) mean (C) for full and geostrophic velocities on the domain shown in Figure 4, computed from the particles launched on a 1 km grid on 15 July 2012 00:00.

In the context of ocean flows, the lack of clustering in divergence-free flows can be verified by considering the geostrophic velocity field. The geostrophic flow can be estimated reasonably easily from synoptic sea surface height measurements and temperature and salinity profiles, unlike the full flow field. In many applications, the geostrophic flow is considered a good approximation to the full flow field, and it has been shown to yield adequate estimates of the stretch deformation patterns [*Olascoaga et al.*, 2013; *Haller and Beron-Vera*, 2013]. Given the theoretical considerations above, however, it is not surprising that the geostrophic approximation to the flow field fails to capture the clustering behavior.

Figure 4 illustrates this point. The top plots compare the full and the geostrophic velocities at one snapshot in time, while the bottom plots show the particle distributions after 10 days. Particles were initialized on a uniform grid and advected by the respective velocity field.

The differences in the velocities are barely noticeable to the eye. Yet the particle distributions have little in common. In particular, the geostrophic velocities do not lead to cluster formation. This is visually obvious and can be verified quantitatively: The maximum cluster strength achieved with the geostrophic approximation is 7.5, whereas with the full velocity field it is 71.2. While only 0.01% of grid points exhibit a cluster strength above 5 after geostrophic advection, 1.78% of grid points do after full advection. Less than 2% may not seem like a large number, but clusters do not dominate the domain; they are isolated, small, but dense structures.

The maximum achieved cluster strength in the domain of interest is more generally useful for summarizing the clustering character of a set of particles quantitatively. Figure 5a shows that it is increasing throughout the 10 day integration period for the example from Figure 4, if the full velocity field is used. It increases slightly from its initial value even in the divergence-free flow, as the initially gridded particles rearrange themselves into a more random distribution.

The mean cluster strength (Figure 5b) remains more or less constant throughout the integration time. There is a small adjustment within the first day for both cases, after which the full velocity integration exhibits a very slight increase. Recall that cluster strength is not strictly conserved, mainly due to edge effects. Figure 5b confirms that these effects remain negligible.

In section 3, the probability distributions of particle pair separations were shown to be consistent with relative dispersion on average coexisting with cluster formation. Particle pair statistics, however, are restricted to original neighbors and are hence limited in their ability to diagnose clusters. These statistics for particles in the nonclustering geostrophic flow follow similar patterns as those for particles in the clustering full flow: the initial delta function centered at 1 km flattens out, with probabilities at both extremes of the spectrum increasing over time, even though clustering is not observed. The distributions do differ, as can be seen in Figure 6, with pair separations more likely to be small in the full flow. However, these small differences hardly indicate the large differences in clustering behavior, as seen in Figures 4 and 5a.
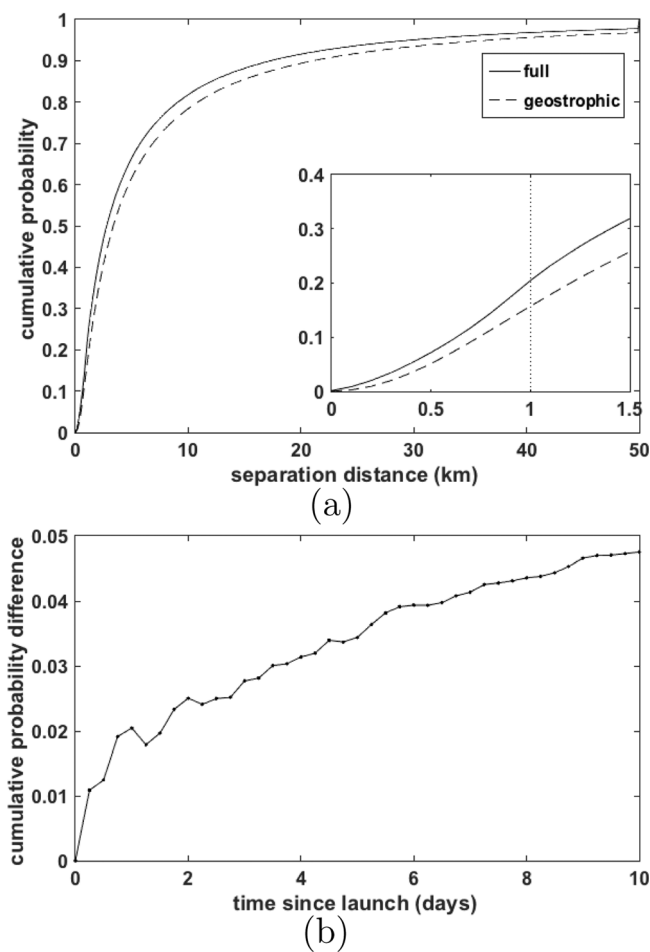
(a)

(b)

Figure 6. (a) Cumulative probability distributions of pair separations after 10 days for full (solid) and geostrophic (dashed) velocity fields. Pairs are defined on the original grid, whereby each particle is partnered with the nearest particle to the north of it. Probabilities are computed using bins with 100 m width. The insert shows the excerpt at the lower end of the scale, with the initial separation distance of 1 km marked as a dotted line. (b) Time series of the difference between the cumulative probability distributions (full minus geostrophic) at 1 km.

Dilation rate has the advantage that it is computed for individual particles, without reliance on neighbors (see Appendix A). The dilation rate field can also be computed on a grid. Just as for the FTLE field, this is accomplished by integrating trajectories initialized at the grid locations backward in time. Figure 7a shows the gridded dilation rate corresponding to the particle distribution shown in Figure 4c. Visually, the patterns delineated by the blue areas in Figure 7a are very similar to those traced out by the particles themselves in Figure 4c and those discernible in the cluster strength in Figure 2.

Figures 7b and 7c show the stretch rate and FTLE, respectively. All three fields exhibit similar patterns. Thus, one might be tempted to conclude that any of these three quantities can serve equally well as a cluster diagnostic. That this is not the case becomes obvious when the geostrophic velocity field is used for the integration. Figure 8 shows the FTLE for the geostrophic case. Since dilation rate is the path-averaged divergence (equation (19)), it is zero up to numerical error for the geostrophic velocity field. Hence also, stretch rate for the geostrophic case is simply twice the FTLE. The field exhibits strong ridges, similar to those in Figure 7, even though there is no discernible clustering (Figure 4d).
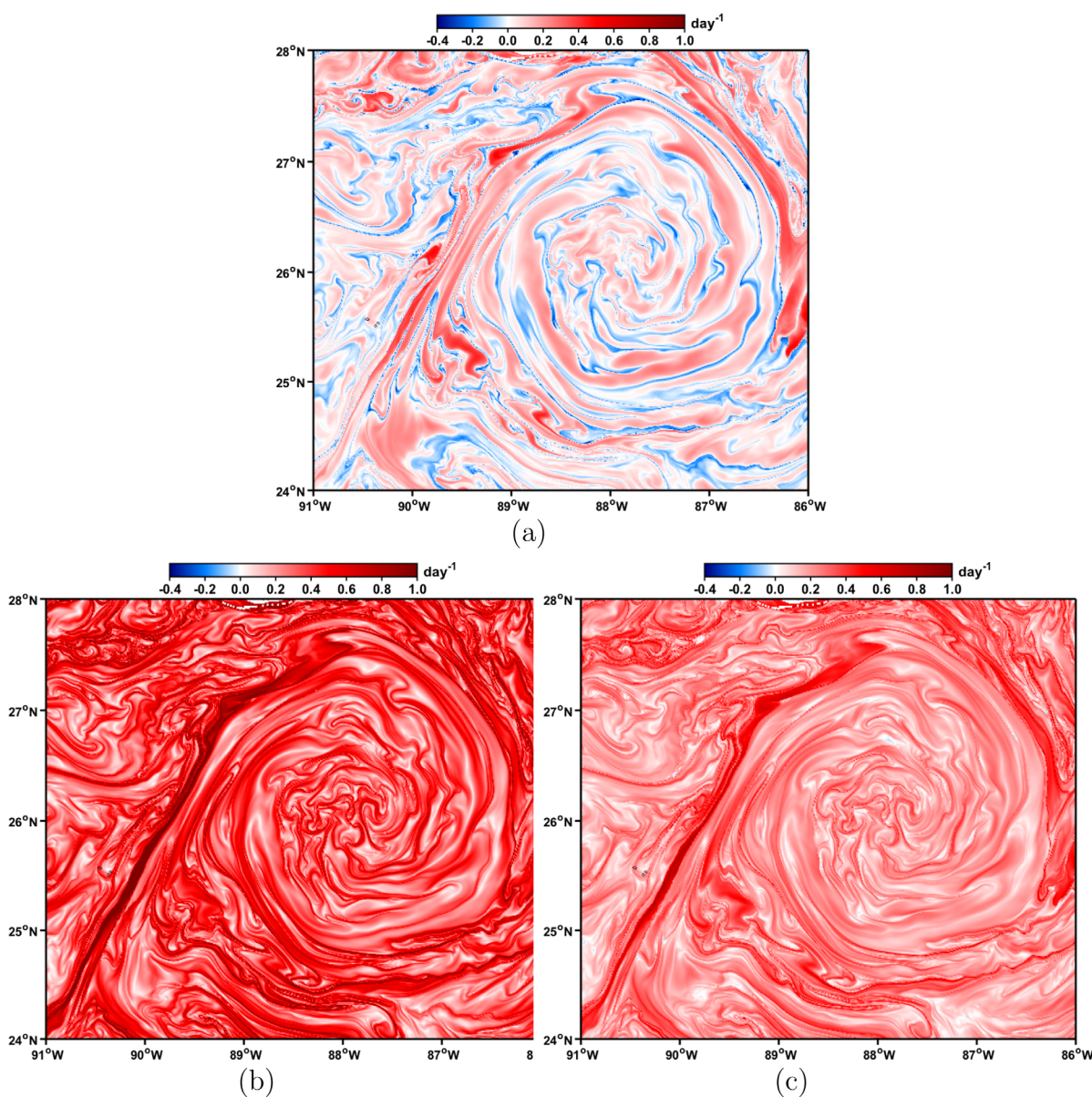
Moreover, the similarity among the dilation rate, stretch rate, and FTLE fields in Figure 7 is not as strong as it appears: note that the correlation between dilation rate and stretch rate is merely -0.04 over the pictured domain. Since stretch generally has a stronger signal than dilation in this region, with greater variance, the variability in the FTLE (recall that it is the average of dilation rate and stretch rate) is dominated by the stretch rate component: the correlation with stretch rate is 0.88, while that with dilation rate is 0.44.

The theory presented in section 4 suggests that clusters should be associated with high negative dilation rates, i.e., particles cluster if they experience large convergence on average over their trajectory. In the computational example, the correlation between cluster strength and dilation rate is -0.57. In comparison, the correlations of cluster strength with FTLE and stretch rate are -0.13 and 0.16, respectively.

Clearly, dilation rate correlates much better with cluster strength than either of the other two metrics. Nonetheless, -0.57 is not a particularly outstanding correlation. This can be explained in part by the nonlinear relationship between cluster strength and dilation rate, as shown in Figure 9.

That figure also suggests that positive dilation rates are much more prevalent than negative ones, at least when considering the entire domain sampled at grid points. In fact, 71% of grid points have *positive* dilation rates. This is another piece of evidence that relative dispersion easily coexists with clustering.

Figure 7. (a) Dilation rate, (b) stretch rate, and (c) FTLE for the time period 15 July 2012 00:00 to 25 July 2012 00:00, computed on a 1 km grid.

If particles preferentially assemble in regions of high negative dilation rate, then the dilation rates sampled by the particles should have a different distribution than those sampled at grid points. This is indeed the case. For the example at hand, 72% of the particles launched on 15 July 2012 on the 1 km grid have experienced total *negative* dilation by 25 July 2012. Thus, negative dilation rate actually has predictive power for particle positions. In other words, areas exhibiting negative dilation rate (here 29%) are more likely (here more than 6 times as likely) to be visited by particles than those with a positive dilation rate.

Dilation rate is not cheap to compute. So the question arises whether one can get away without integrating divergence along trajectories (see Appendix A for the actual algorithm) and simply use instantaneous divergence, as suggested by *Zhong et al.* [2012]. Figure 10 displays the divergence field at the end of the integration time period, 25 July 2012. It is not as smooth as the Lagrangian fields, but it does contain the strong linear feature in the southwest quadrant of the displayed domain. In this domain, 51% of the area experiences negative divergence. Of the particles launched on 15 July 2012 that were in this domain on 25 July 2012, 58% land in regions of negative divergence. So there is indeed a small sampling bias toward
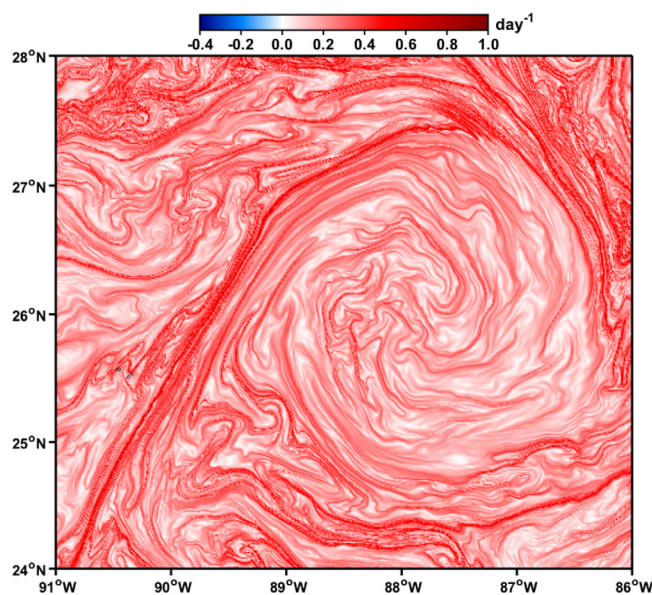
Figure 8. FTLE for the time period 15 July 2012 00:00 to 25 July 2012 00:00, computed on a 1 km grid, using geostrophic velocities.

convergence, but not nearly as strong as for dilation rate. The predictive power of divergence for particle positions is thus small. Nor does divergence correlate well with cluster strength: the correlation is −0.09. Clearly, the computational shortcut of ignoring a particle's past does not lead to satisfactory results for integration periods this long.

6. Conclusions

Identifying regions of clustering in the ocean is of interest for various reasons: these regions often exhibit interesting dynamics. They are biologically important, as they can aggregate nutrients. For pollution response, they are critical, as they indicate where the clean-up can be most efficient. In this work, we have provided a rigorous definition of "clustering," along with a metric to determine a degree of clustering. We have posited a predictive relationship between dilation and clustering strength, based on theory. Within the context of a numerical example in a realistic ocean model, this relationship was shown to hold. While advected material preferentially occupies regions of negative dilation rate, most of the model ocean exhibits positive dilation rate, consistent with the well-established average dispersion behavior.

For the aggregation of material, convergence is clearly critical. Clustering, however, is an integrative process, and thus dilation, the path-integrated divergence, is more appropriate as a diagnostic than instantaneous Eulerian divergence.
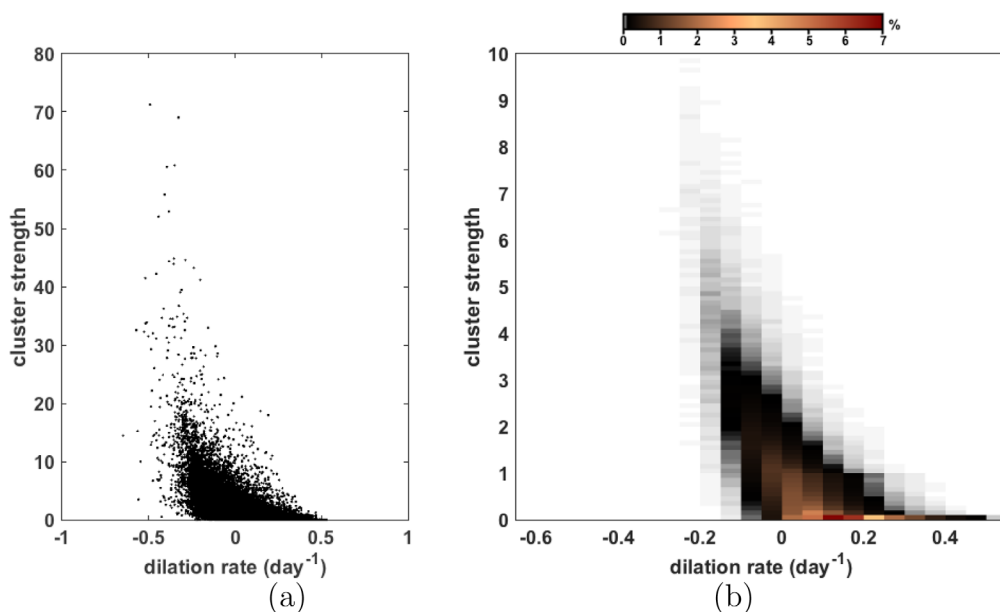

Figure 9. (a) Scatterplot of cluster strength as a function of dilation rate computed for the 10 day integration from 15 July 2012 to 25 July 2012 on a 1 km grid over the domain shown in Figure 4. (b) Two-dimensional histogram of the same data (with cluster strength capped at 10), expressed as a percentage of the total number of samples.
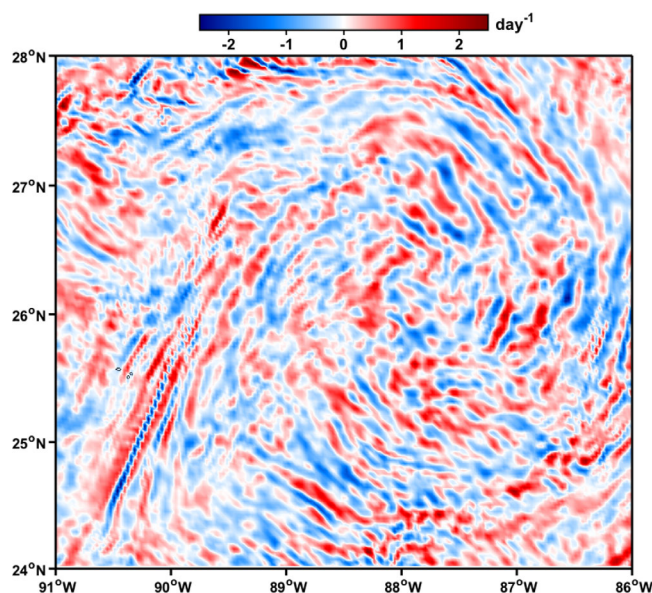
Figure 10. Instantaneous divergence on 25 July 2012 00:00.

Maps of dilation provide an excellent guide to where clusters of advected particles, that were initially uniformly spaced, will be found. Nonetheless, it is important to remember that the locations of the clusters are not necessarily places of local convergence. Aggregated material continues to be advected, stretched into different shapes, pulled apart, and reassembled. What makes dilation such a powerful diagnostic is its ability to capture the cumulative effects of these processes on cluster positioning.

The most straightforward method for identifying cluster locations developing from a uniform distribution in a model is to simply advect a large number of particles. To compute dilation, the divergence field has to be integrated along trajectories. So what is gained by adding this additional step to the calculation? The main advantage is that a much coarser grid of trajectories can be used, requiring far fewer integrations, because a single along-trajectory integration provides the dilation at that point, whereas cluster strength requires a whole field of particles to be meaningful. Moreover, by employing integrations backward in time, dilation can be computed for a target area without seeding a much larger region that may or may not contribute to clustering in the target area. Such backward integrations cannot be leveraged for direct particle advections. (This latter advantage becomes less relevant in the context of clusters evolving from initially non-uniformly distributed material, a case not presented here.)

While the aggregation process is most relevant for cluster identification, deformation also includes stretching processes. Here we have only made preliminary inquiries into the relationship between stretch and dilation. The patterns exhibited in the numerical example for the two fields are visually remarkably similar, yet show very low correlation. This raises interesting questions about the connections between the two fields, both statistically and physically. Strong lines of stretching may, for example, also be associated with strong dilation; if the relationship is nonlinear, correlation is not the best metric to tease this out. The correlation may also be scale dependent or require a spatial lag. Future work will delve further into these topics.

A shortcoming of dilation is that it provides no insight into the physical processes responsible for the cluster formation. In fact, its strength of reflecting cumulative effects, which is critical for a diagnostic, makes the identification of these challenging. These aspects are addressed by *Jacobs et al.* [2015].

Most observed clusters originate from nonuniformly distributed material. Advection is not the only process responsible for forming clusters; biology and chemistry also have a role to play. These aspects have been neglected in the analysis presented here. How effective dilation maps can be in tracing accumulation regions of nonuniformly initialized material remains a subject of active inquiry.

Appendix A: Computing Dilation and Related Quantities

Dilation is the product of the singular values of the deformation tensor $\boldsymbol{F}$ (see equation (11)). Since $\boldsymbol{F}$ is a 2 × 2 matrix (see equation (9)), the singular values can be derived using an analytic formula. Thus, the primary challenge is to compute the deformation tensor itself. Traditionally, this has been achieved using a finite difference algorithm for each of the partial derivatives [*Lekien et al.*, 2005; *Branicki and Wiggins*, 2010]. The problem with this approach is that a fairly dense grid of trajectories is needed for an accurate approximation. Alternatively, each point on a coarser grid requires the integration of four additional trajectories at subgrid spacing [*Beron-Vera et al.*, 2008].

This increased computational cost can be avoided by rewriting the problem as an integral:

$$F_{ij} = \frac{\partial x_i}{\partial x_{0j}} = \delta_{ij} + \int_0^t \frac{\partial u_i}{\partial x_{0j}} d\tau, \tag{A1}$$

which follows directly from equation (8). By the chain rule, this then becomes

$$F_{ij} = \delta_{ij} + \int_0^t \left(\sum_{k=1}^{2} \frac{\partial u_i}{\partial x_k} \frac{\partial x_k}{\partial x_{0j}} \right) d\tau, \tag{A2}$$

$$= \delta_{ij} + \int_0^t \left(\sum_{k=1}^{2} \frac{\partial u_i}{\partial x_k} F_{kj} \right) d\tau. \tag{A3}$$

Now the components of the deformation tensor can be computed using numerical quadrature. The integration is performed along the trajectory, which is computed first by integrating the path equation (8). For the calculations used here, we chose a fixed-step fourth-order Runge-Kutta scheme with a 10 min time step for both integrations. Velocities and velocity gradients are interpolated trilinearly, in space and time, to the particle positions. Velocity gradients are approximated from gridded velocities using the second-order centered finite difference scheme.

The product of the singular values of a square matrix is also identical to the absolute value of its determinant. Thus, we compute dilation as the determinant of $\mathbf{F}$. To compute the FTLE, we find the leading singular value using the analytic formula for a 2×2 matrix. There are well-known challenges with establishing the smaller singular value accurately using the analytic expression, since it involves subtracting two terms that may both be large, but whose difference may be small and hence subject to substantial numerical error. Instead, we divide the determinant by the leading singular value, an approach that is more robust to numerical error.

References

Barron, C. N., A. B. Kara, P. J. Martin, R. C. Rhodes, and L. F. Smedstad (2006), Formulation, implementation and examination of vertical coordinate choices in the Global Navy Coastal Ocean Model (NCOM), *Ocean Model.*, *11*(3-4), 347–375, doi:10.1016/j.ocemod.2005.01.004.

Barron, C. N., A. B. Kara, R. C. Rhodes, C. Rowley, and L. F. Smedstad (2007), Validation test report for the 1/8° Global Navy Coastal Ocean Model Nowcast/Forecast System, *Tech. Rep. NRL/MR/7320–07-9019*, Nav. Res. Lab., Stennis Space Center, Miss.

Beron-Vera, F. J., M. J. Olascoaga, and G. J. Goni (2008), Oceanic mesoscale eddies as revealed by Lagrangian coherent structures, *Geophys. Res. Lett.*, *35*, L12603, doi:10.1029/2008GL033957.

Boffetta, G., G. Lacorata, G. Radaelli, and A. Vulpiani (2001), Detecting barriers to transport: A review of different techniques, *Physica D*, *159*(1-2), 58–70, doi:10.1016/S0167-2789(01)00330-X.

Boffetta, G., F. De Lillo, and A. Gamba (2004), Large scale inhomogeneity of inertial particles in turbulent flows, *Phys. Fluids*, *16*(4), L20–L23, doi:10.1063/1.1667807.

Branicki, M., and S. Wiggins (2010), Finite-time Lagrangian transport analysis: Stable and unstable manifolds of hyperbolic trajectories and finite-time Lyapunov exponents, *Nonlinear Processes Geophys.*, *17*(1), 1–36, doi:10.5194/npg-17-1-2010.

Coulliette, C., F. Lekien, J. D. Paduan, G. Haller, and J. E. Marsden (2007), Optimal pollution mitigation in Monterey Bay based on coastal radar data and nonlinear dynamics, *Environ. Sci. Technol.*, *41*(18), 6562–6572, doi:10.1021/es0630691.

Cressman, J. R., J. Davoudi, W. I. Goldburg, and J. Schumacher (2004), Eulerian and Lagrangian studies in surface flow turbulence, *New J. Phys.*, *6*(1), 53, doi:10.1088/1367-2630/6/1/053.

Cummings, J. A. (2005), Operational multivariate ocean data assimilation, *Q. J. R. Meteorol. Soc.*, *131*(613), 3583–3604, doi:10.1256/qj.05.105.

Day, R. H., and D. G. Shaw (1987), Patterns in the abundance of pelagic plastic and tar in the north Pacific Ocean, 1976-1985, *Mar. Pollut. Bull.*, *18*(6B), 311–316, doi:10.1016/S0025-326X(87)80017-6.

Dempster, A. P., N. M. Laird, and D. B. Rubin (1977), Maximum likelihood from incomplete data via the EM algorithm, *J. R. Stat. Soc., Ser. B*, *39*(1), 1–38.

d'Ovidio, F., V. Fernández, E. Hernández-García, and C. López (2004), Mixing structures in the Mediterranean Sea from finite-size Lyapunov exponents, *Geophys. Res. Lett.*, *31*, L17203, doi:10.1029/2004GL020328.

Fiabane, L., R. Zimmermann, R. Volk, J.-F. Pinton, and M. Bourgoin (2012), Clustering of finite-size particles in turbulence, *Phys. Rev. E, 86*, 035301(R), doi:10.1103/PhysRevE.86.035301.

Haller, G. (2001), Distinguished material surfaces and coherent structures in three-dimensional fluid flows, *Physica D*, *149*(4), 248–277, doi:10.1016/S0167-2789(00)00199-8.

Haller, G. (2002), Lagrangian coherent structures from approximate velocity data, *Phys. Fluids*, *14*(6), 1851–1861, doi:10.1063/1.1477449.

Haller, G., and F. J. Beron-Vera (2012), Geodesic theory of transport barriers in two-dimensional flows, *Physica D*, *241*(20), 1680–1702, doi:10.1016/j.physd.2012.06.012.

Haller, G., and F. J. Beron-Vera (2013), Coherent Lagrangian vortices: The black holes of turbulence, *J. Fluid Mech.*, *731*, R4, doi:10.1017/jfm.2013.391.

Haller, G., and G.-C. Yuan (2000), Lagrangian coherent structures and mixing in two-dimensional turbulence, *Physica D*, *147*(3-4), 352–370, doi:10.1016/S0167-2789(00)00142-1.

Harrison, C. S., and G. A. Glatzmaier (2012), Lagrangian coherent structures in the California Current System—Sensitivities and limitations, *Geophys. Astrophys. Fluid Dyn.*, *106*(1), 22–44, doi:10.1080/03091929.2010.532793.

Hernández-Carrasco, I., C. López, E. Hernández-García, and A. Turiel (2011), How reliable are finite-size Lyapunov exponents for the assessment of ocean dynamics?, *Ocean Model.*, *36*, 208–218, doi:10.1016/j.ocemod.2010.12.006.

Hodur, R. M. (1997), The Naval Research Laboratory's coupled ocean/atmosphere mesoscale prediction system (COAMPS), *Mon. Weather Rev.*, *125*(7), 1414–1430, doi:10.1175/1520-0493(1997)125<1414:TNRLSC>2.0.CO;2.

Hodur, R. M., X. Hong, J. D. Doyle, J. Pullen, J. A. Cummings, P. J. Martin, and M. A. Rennick (2002), The coupled ocean/atmosphere meso-scale prediction system (COAMPS), *Oceanography*, *15*(1), 88–98, doi:10.5670/oceanog.2002.39.

Howell, E. A., S. J. Bograd, C. Morishige, M. P. Seki, and J. J. Polovina (2012), On North Pacific circulation and associated marine debris concentration, *Mar. Pollut. Bull.*, *65*(1-3), 16–22, doi:10.1016/j.marpolbul.2011.04.034.

Huntley, H. S., B. L. Lipphardt Jr., and A. D. Kirwan Jr. (2011), Surface drift predictions of the *Deepwater Horizon* spill: The Lagrangian perspective, in *Monitoring and Modeling the Deepwater Horizon Oil Spill: A Record-Breaking Enterprise*, edited by Y. Liu et al., pp. 179–195, AGU, Washington, D. C., doi:10.1029/2011GM001097.

Jacobs, G. A., H. S. Huntley, A. D. Kirwan Jr., B. L. Lipphardt Jr., T. Campbell, T. Smith, K. Edwards, B. Bartels, and A. Haza (2015), Ocean processes underlying surface clustering, *J. Geophys. Res. Oceans*, in press.

Johnson, S. (1967), Hierarchical clustering schemes, *Psychometrika*, *32*(3), 241–254, doi:10.1007/BF02289588.

Kaiser, J. (2010), The dirt on ocean garbage patches, *Science*, *328*(5985), 1506, doi:10.1126/science.328.5985.1506.

Klyatskin, V. I., and A. I. Saichev (1997), Statistical theory of the diffusion of a passive tracer in a random velocity field, *J. Exp. Theor. Phys.*, *84*(4), 716–724, doi:10.1134/1.558205.

Koszalka, I. M., and J. H. LaCasce (2010), Lagrangian analysis by clustering, *Ocean Dyn.*, *60*(4), 957–972, doi:10.1007/s10236-010-0306-2.

Koszalka, I. M., J. H. LaCasce, M. Andersson, K. A. Orvik, and C. Mauritzen (2011), Surface circulation in the Nordic Seas from clustered drifters, *Deep Sea Res., Part I*, *58*(4), 468–485, doi:10.1016/j.dsr.2011.01.007.

Lebreton, L. C.-M., S. D. Greer, and J. C. Borrero (2012), Numerical modelling of floating debris in the world's oceans, *Mar. Pollut. Bull.*, *64*(3), 653–661, doi:10.1016/j.marpolbul.2011.10.027.

Lekien, F., C. Coulliette, A. J. Mariano, E. H. Ryan, L. K. Shay, G. Haller, and J. E. Marsden (2005), Pollution release tied to invariant manifolds: A case study for the coast of Florida, *Physica D*, *210*(1–2), 1–20, doi:10.1016/j.physd.2005.06.023.

Lloyd, S. P. (1982), Least squares quantization in PCM, *IEEE Trans. Inf. Theory*, *28*(2), 129–137, doi:10.1109/TIT.1982.1056489.

Mancho, A. M., D. Small, and S. Wiggins (2006), A tutorial on dynamical systems concepts applied to Lagrangian transport in oceanic flows defined as finite time data sets: Theoretical and computational issues, *Phys. Rep.*, *437*(3-4), 55–124, doi:10.1016/j.physrep.2006.09.005.

Mendoza, C., and A. M. Mancho (2010), Hidden geometry of ocean flows, *Phys. Rev. Lett.*, *105*(3), 038501, doi:10.1103/PhysRevLett.105.038501.

Mezić, I., S. Loire, V. A. Fonoberov, and P. J. Hogan (2010), A new mixing diagnostic and Gulf oil spill movement, *Science*, *330*(6003), 486–489, doi:10.1126/science.1194607.

Monchaux, R., M. Bourgoin, and A. Cartellier (2010), Preferential concentration of heavy particles: A Voronoï analysis, *Phys. Fluids*, *22*(10), 103304, doi:10.1063/1.3489987.

Olascoaga, M. J., and G. Haller (2012), Forecasting sudden changes in environmental pollution patterns, *Proc. Natl. Acad. Sci. U. S. A.*, *109*(13), 4738–4743, doi:10.1073/pnas.1118574109.

Olascoaga, M. J., et al. (2013), Drifter motion in the Gulf of Mexico constrained by altimetric Lagrangian coherent structures, *Geophys. Res. Lett.*, *40*, 6171–6175, doi:10.1002/2013GL058624.

Poje, A. C., A. C. Haza, T. M. Özgökmen, M. G. Magaldi, and Z. D. Garraffo (2010), Resolution dependent relative dispersion statistics in a hierarchy of ocean models, *Ocean Model.*, *31*(1-2), 36–50, doi:10.1016/j.ocemod.2009.09.002.

Poje, A. C., et al. (2014), Submesoscale dispersion in the vicinity of the *Deepwater Horizon* spill, *Proc. Natl. Acad. Sci. U. S. A.*, *111*(35), 12,693–12,698, doi:10.1073/pnas.1402452111.

Rypina, I. I., L. J. Pratt, J. Pullen, J. Levin, and A. L. Gordon (2010), Chaotic advection in an archipelago, *J. Phys. Oceanogr.*, *40*(9), 1988–2006, doi:10.1175/2010JPO4336.1.

Samelson, R. M. (2013), Lagrangian motion, coherent structures, and lines of persistent material strain, *Annu. Rev. Mar. Sci.*, *5*, 137–163, doi:10.1146/annurev-marine-120710-100819.

Sawford, B. (2001), Turbulent relative dispersion, *Annu. Rev. Fluid Mech.*, *33*(1), 289–317, doi:10.1146/annurev.fluid.33.1.289.

Schumacher, J., and B. Eckhardt (2002), Clustering dynamics of Lagrangian tracers in free-surface flows, *Phys. Rev. E*, *66*(1), 017303, doi:10.1103/PhysRevE.66.017303.

Shadden, S. C., F. Lekien, and J. E. Marsden (2005), Definition and properties of Lagrangian coherent structures from finite-time Lyapunov exponents in two-dimensional aperiodic flows, *Physica D*, *212*(3-4), 271–304, doi:10.1016/j.physd.2005.10.007.

Toner, M., A. D. Kirwan Jr., A. C. Poje, L. H. Kantha, F. E. Müller-Karger, and C. K. R. T. Jones (2003), Chlorophyll dispersal by eddy-eddy interactions in the Gulf of Mexico, *J. Geophys. Res.*, *108*(C4), 3105, doi:10.1029/2002JC001499.

Yoder, J. A., S. G. Ackleson, R. T. Barber, P. Flament, and W. M. Balch (1994), A line in the sea, *Nature*, *371*(6499), 689–692, doi:10.1038/371689a0.

Zhong, Y., A. Bracco, and T. A. Villareal (2012), Pattern formation at the ocean surface: Sargassum distribution and the role of the eddy field, *Limnol. Oceanogr. Fluids Environ.*, *2*, 12–27, doi:10.1215/21573689-1573372.